

Wide-field extended-resolution fluorescence microscopy with standing surface plasmon resonance waves

Euiheon Chung^{1,2}, Yang-Hyo Kim¹, Wai Teng Tang³, Colin J. R. Sheppard⁴, and

Peter T. C. So^{1,5*}

¹*Department of Mechanical Engineering, Massachusetts Institute of Technology, 77
Massachusetts Avenue, Cambridge, MA 02139, USA*

²*Edwin L. Steele laboratory, Department of Radiation Oncology, Massachusetts General
Hospital, Boston, MA 02114, USA*

³*Computation and Systems Biology, Singapore-MIT Alliance, National University of Singapore,
4 Engineering Drive 3, Singapore 117576, Singapore*

⁴*Division of Bioengineering, National University of Singapore, 9 Engineering Drive 1,
Singapore 117576, Singapore*

⁵*Department of Biological Engineering, Massachusetts Institute of Technology, 77
Massachusetts Avenue, Cambridge, MA 02139*

*Corresponding author: ptso@mit.edu

The resolution of conventional SPR imaging has been limited by the diffraction nature of light. A wide-field extended-resolution optical imaging technique, standing-wave surface plasmon resonance fluorescence (SW-SPRF) microscopy, has been developed. Based on evanescent SPR standing waves, SW-SPRF provides lateral resolution approaching 100 nm and offers the advantages of significant signal enhancement and background noise reduction. SW-SPRF has the potential for sensitive biomolecular detection, nanoscale imaging, and lithographic applications. ©2009 Optical Society of America

OCIS codes: 180.0180, 180.2520, 180.3170, 240.6680, 260.6970

The concept of a perfect lens realized with negative refractive index materials was recently proposed [1]. Surface plasmon resonance (SPR) – resonant energy transfer from incident photons to electron density oscillations along a metal-dielectric interface – helps to enhance weak evanescent waves, which essentially carry the high spatial frequency information, thereby improving the imaging resolution. However, a limitation of this approach is that the detection must be done in the near-field [2]. Recent work demonstrated that far-field detection is possible with periodic corrugations in the metal layer [3], and that magnification can similarly be achieved [4]. While super-resolution on the order of $\lambda/4$ can be obtained with these methods, the sample must be placed at a specific location that is virtually impossible for most biomedical applications. Further, these methods require substrate with very specific and high-resolution patterns increasing system cost. In this Letter sub-diffraction imaging using standing-wave surface plasmon resonance fluorescence (SW-SPRF) microscopy is demonstrated with enhanced contrast. SW-SPRF operates in wide-field, without the need of complex substrate fabrication, and provides lateral resolution approaching 100 nm.

A schematic of the SW-SPRF microscope is shown in Fig. 1. In this configuration, counter-propagating SPR waves are launched through a high NA objective lens, which interfere and excite fluorophores close to the metal interface. Emission light is collected via the objective. This setup employs a phenomenon known as surface plasmon-coupled emission (SPCE) or surface plasmon resonance fluorescence (SPRF) [5-7]. It dispenses with the traditional Kretschmann-Raether prism-based configuration and simplifies overall system design. Furthermore, SPRF provides several advantages compared with total internal reflection fluorescence (TIRF) including better background suppression, smaller detection volume, and

decreased fluorescence lifetime and photobleaching [8]. In Fig. 1, a linear polarizer between the collimation lens and the tube lens selects either *s*- or *p*- polarized (-pol) illumination. A thin gold film (40 ± 2.3 nm) was prepared on coverslips by vapor deposition (EMF Corp., Ithaca, NY) and the gold film was covered with a layer of silica (SiO_x, 5 nm). Thickness of the film was confirmed by AFM and ellipsometry. Diluted solution containing sub-diffraction size fluorescent beads (diameter 0.04 μm; Molecular Probes, OR) was spread on the gold-coated coverslip and dried overnight. Subsequently, two beams propagating through the objective lens are interfered and excite the sample on the metal coated coverslip. The angles of incidence of both beams are fixed at the SPR angle of 44.7°. The images were then collected by an intensified CCD. The SW phase was controlled by a feedback control system that was functional with *p*-pol standing wave [9].

Due to electromagnetic boundary conditions, surface plasmons can only be excited by *p*-pol illumination. With two counter-propagating *p*-pol beams, an expression of the intensity of the interfered beams can be obtained as

$$I_{SW-SPRF} = 2|t_p(\theta)|^2 \exp\left(-\frac{z}{\delta}\right) (2 \sin^2 \theta - \beta^2) \times \left[1 - \left(\frac{\beta^2}{2 \sin^2 \theta - \beta^2} \right) \cos(2kx \sin \theta) \right]$$

where t_p denotes the three-layer Fresnel coefficient, θ is the incident angle, δ is the penetration depth, k the wave vector in the immersion medium, and β is the ratio of the refractive indices between the sample and immersion medium. Unlike SW- TIRF illumination with *s*-pol, where the contrast ratio is 1 for all incident angles and medium, *p*-pol SW-SPR illumination results in a contrast ratio as a function of the incident angle and the refractive indices. Thus, optimizing image contrast requires careful selection of incident angle. At the SPR angle of 44.7°, the

contrast ratio is close to 0.8. Fig. 2 shows a plot of the contrast ratio as the incident angle is varied.

The procedure of generating extended-resolution images with SW-SPRF in the vertical direction is shown in Fig. 3. Due to the unique doughnut-shape point-spread function (PSF) of SPRF [7], there exists a central dip in the PSF and the overall full-width-at-half-maximum (FWHM) becomes widened. A non-linear deconvolution algorithm was applied to convert the doughnut-shape SPRF PSF in Fig. 3(a2) into a more conventional Airy disk shape PSF as shown in Fig. 3(b2). Based on our numerical model of the PSF, the Richardson-Lucy algorithm was used with the theoretical PSF kernel as an input. The deconvolution procedure also slightly improves signal-to-noise ratio by a factor of two.

To generate a SW-SPRF image, three intermediate SPRF images (denoted as “Orig SPRF”; one representative image shown in Fig. 3(a1)) are taken at three SW phases (0 , $2\pi/3$, and $4\pi/3$) as in SW-TIRF imaging. Then, the deconvolution algorithm is applied to convert the original doughnut-shape PSFs into PSFs that are single-lobed (“Decon SPRF”, Fig. 3(b2)) followed by the application of the SW-TIRF algorithm [10]. These three deconvolved SPRF images are used to generate one enhanced image (“Decon SW-SPRF”, Fig. 3(c1)). The side band of SW-SPRF in Fig. 3(c2) can be removed with simple linear deconvolution (“Decon SW-SPRD”) as shown in Fig. 3(d2). The PSF profiles in Fig. 3(c2) and 3(d2) demonstrate that the FWHMs of both SW-SPRF and SW-SPRD are more than a factor of two narrower than that of the deconvolved SPRF PSF in Fig. 3(b2) and approximately four times narrower than that of the original SPRF PSF in Fig. 3(a2). The bandwidth of the current setup is slightly narrower than TIRF system due to the lower incidence angle set by the SPR condition, however this effect can be negligible in silver/water interface with higher SPR angle ($\sim 70^\circ$). Although one directional

resolution enhancement has been demonstrated here, two-dimensional imaging with extended-resolution in both directions is also possible [9, 11]. We also compared the intensity of the fluorescent beads spread on the gold-coated coverslip under SPRF conditions as well as on the bare coverslip under TIRF conditions. Typical bead images under each of the four imaging conditions – SPRF with *p*- or *s*-pol, TIRF with *p*- or *s*-pol illumination, are shown in Fig. 4(a) to 4(d). For clarity, these comparisons were performed with non-standing wave illumination by blocking the incoming beam from one of the fiber tips. The PSF of SPRF (*p*-pol) shows a significantly stronger signal with a doughnut-shape intensity distribution. In contrast, as surface plasmons cannot be excited with *s*-pol excitation, no beads appear in Fig. 4(b). The average intensity detected for each imaging condition was quantified using the same incident power and corresponding background subtraction (Fig. 4(e)). The integrated intensity signals were obtained from within the first maximum ring of the SPRF PSF images. On average, SPRF (*p*-pol) shows more than four times enhancement compared with TIRF (*p*-pol) while TIRF (*p*-pol) shows about 40% higher intensity than TIRF (*s*-pol). Both of the differences are statistically significant by Student's *t* test ($p < .001$). It is noted that SPRF signal enhancement was not predicted with simulation without considering surface roughness [12].

In summary, sub-diffraction-limited resolution is achieved with standing surface plasmon resonance waves. SW-SPRF also shows a significant increase in signal-to-background ratio. While SW-SPRF retains the advantages of SPCE including decreased fluorescence lifetime and thus reduced photobleaching for biological imaging, it does not suffer from low spatial resolution. The PSF of SW-SPRF is four times narrower than typical SPCE. The use of silver instead of gold, together with optimized surface roughness and thickness of the silica layer may lead to even greater signal enhancement [8]. Moreover, the use of metal gratings has a potential

for further resolution enhancement [13]. SW-SPRF may be useful in applications requiring both high signal-to-noise ratio and high spatial resolution such as in biomolecular sensing, imaging, and nano-scale lithography [14].

This research was funded by the National Science Foundation (MCB-9604382) and the National Institutes of Health (P01HL64858). The authors thank Sunyoung Lee, Kimin Jun, and Seung Woo Lee of MIT for assisting AFM and ellipsometry measurements.

References

1. J. B. Pendry, "Negative refraction makes a perfect lens," *Phys Rev Lett* **85**, 3966-3969 (2000).
2. N. Fang, H. Lee, C. Sun, and X. Zhang, "Sub-Diffraction-Limited Optical Imaging with a Silver Superlens," *Science* **308**, 534-537 (2005).
3. Z. Liu, S. Durant, H. Lee, Y. Pikus, N. Fang, Y. Xiong, C. Sun, and X. Zhang, "Far-field optical superlens," *Nano Lett* **7**, 403-408 (2007).
4. I. I. Smolyaninov, Y. Huang and C. C. Davis, "Magnifying Superlens in the Visible Frequency Range," *Science* **315**, 1699 (2008).
5. J. Borejdo, Z. Gryczynski, N. Calander, P. Muthu, and I. Gryczynski, "Application of surface plasmon coupled emission to study of muscle," *Biophysical Journal* **91**, 2626-2635 (2006).
6. T. P. Burghardt, J. E. Charlesworth, M. F. Halstead, J. E. Tarara, and K. Ajtai, "In Situ Fluorescent Protein Imaging with Metal Film Enhanced Total Internal Reflection Microscopy," *Biophysical Journal* **90**, 4662-4671 (2006).
7. W. T. Tang, Chung, E., Kim, Y., So, P. T. C., Sheppard, C. J. R., "Investigation of the Point Spread Function of Surface Plasmon-Coupled Emission Microscopy," *Optics Express* (2007).
8. J. Borejdo, N. Calander, Z. Gryczynski, and I. Gryczynski, "Fluorescence correlation spectroscopy in surface plasmon coupled emission microscope," *Optics Express* **14**, 7878-7888 (2006).
9. E. Chung, D. Kim, Y. Cui, Y.-H. Kim, and P. T. C. So, "Two-Dimensional Standing Wave Total Internal Reflection Fluorescence Microscopy: Superresolution Imaging of Single Molecular and Biological Specimens," *Biophys. J.* **93**, 1747-1757 (2007).

10. P. T. C. So, H. S. Kwon, and C. Y. Dong, "Resolution enhancement in standing-wave total internal reflection microscopy: a point-spread-function engineering approach," *Journal Of The Optical Society Of America A-Optics Image Science And Vision* **18**, 2833-2845 (2001).
11. R. Fiolka, M. Beck, and A. Stemmer, "Structured illumination in total internal reflection fluorescence microscopy using a spatial light modulator," *Opt Lett* **33**, 1629-1631 (2008).
12. J. Enderlein, and T. Ruckstuhl, "The efficiency of surface-plasmon coupled emission for sensitive fluorescence detection," *Optics Express* **13**, 8855-8865 (2005).
13. H. Raether, *Surface plasmons on smooth and rough surfaces and on gratings* (Springer-Verlag, Berlin ; New York :, 1987).
14. Z. W. Liu, Q. H. Wei, and X. Zhang, "Surface plasmon interference nanolithography," *Nano Letters* **5**, 957-961 (2005).

References

1. J. B. Pendry, Phys. Rev. Lett. 85, 3966 (2000).
2. N. Fang, H. S. Lee, C. Sun and X. Zhang, Science 308, 534, (2005).
3. Z. Liu, S. Durant, H. Lee, Y. Pikus, N. Fang, Y. Xiong and X, Zhang, Nano Lett. **7**, 403 (2007).
4. I. I. Smolyaninov, Y. Huang and C. C. Davis, Science 315, 1699 (2008).
5. J. Borejdo, Z. Gryczynski, N. Calander, P. Muthu, and I. Gryczynski, Biophys. J. **91**, 2626 (2006).
6. T. P. Burghadt, , J. E. Charlesworth, M. F. Halstead, J. E. Tarara and J. Ajtai, Biophys J. **90**, 4662-4671 (2006).
7. W. T. Tang, E. Chung, Y.-H. Kim, P. T. C. So, C. J. R. Sheppard, Opt. Express **15**, 4634 (2007).
8. J. Borejdo, N. Calander, Z. Gryczynski, and I. Gryczynski, Opt. Express **14**, 7878 (2006).
9. E. Chung, D. Kim, Y. Cui, Y.-H. Kim, and P. T. C. So, Biophys. J. **93**, 1747 (2007).
10. P. T. C. So, H. S. Kwon, and C. Y. Dong, J. Opt. Soc. Am. A **18**, 2833 (2001).
11. R. Fiolka, M. Beck, and A. Stemmer, Opt Lett **33**, 1629-1631 (2008)
12. J. Enderlein, and T. Ruckstuhl, Opt. Express **13**, 8855 (2005).
13. H. Raether, *Surface Plasmons on Smooth and Rough Surfaces and on Gratings*, (Springer-Verlag, 1986).
14. Z. W. Liu, Q. H. Wei, and X. Zhang, "Surface plasmon interference nanolithography," Nano Lett. **5**, 957 (2005).

Figure Captions

Fig. 1. Experimental setup of standing-wave surface plasmon resonance fluorescence (SW-SPRF) microscopy

Fig. 2. Contrast of *p*-polarized evanescent standing waves with immersion medium refractive index ~ 1.515 and three different sample medium – air ($n = 1.0$), water ($n = 1.33$) and cellular cytoplasm ($n \sim 1.38$)

Fig. 3. Extended-resolution imaging with standing-wave surface plasmon resonance fluorescence (SW-SPRF) microscopy in vertical direction (a1) original SPRF image with doughnut-shape PSF, (b1) deconvolved SPRF image, (c1) SW-SPRF image after applying the SW-TIRF algorithm on three deconvolved SPRF images, (d1) SW-SPRF image with linear deconvolution to reduce side lobes; (a2)-(d2) comparison of PSF profiles of various imaging methods at a selected region of interest (ROI). Scale bar: 2 μm . Inset size: 1.3 μm across.

Fig. 4. Comparison of various imaging modes (a)-(d) Images of fluorescent beads under different imaging conditions with the same incident angle, excitation intensity, and exposure time. Scale bar: 2 μm and Inset: 2.5 μm across. (e) Comparison of intensity of fluorescent beads under various imaging modes. ($n = 48$ each, standard error)

Figures

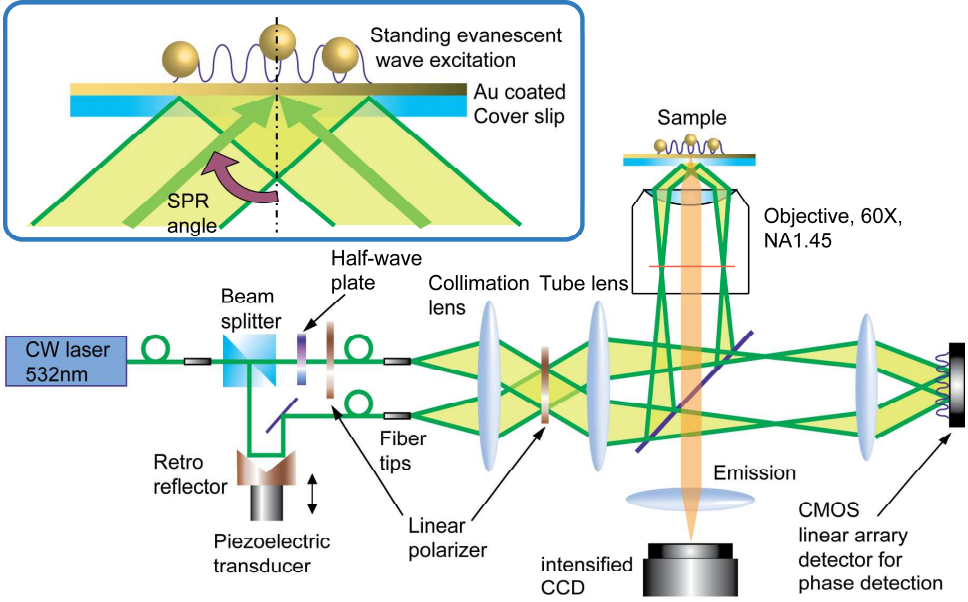


Fig. 1. Experimental setup of standing-wave surface plasmon resonance fluorescence (SW-SPRF) microscopy

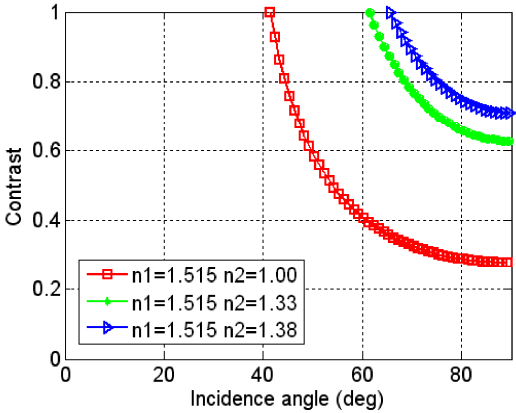


Fig. 2. Contrast of *p*-polarized evanescent standing waves with immersion medium refractive index ~ 1.515 and three different sample medium – air ($n = 1.0$), water ($n = 1.33$) and cellular cytoplasm ($n \sim 1.38$)

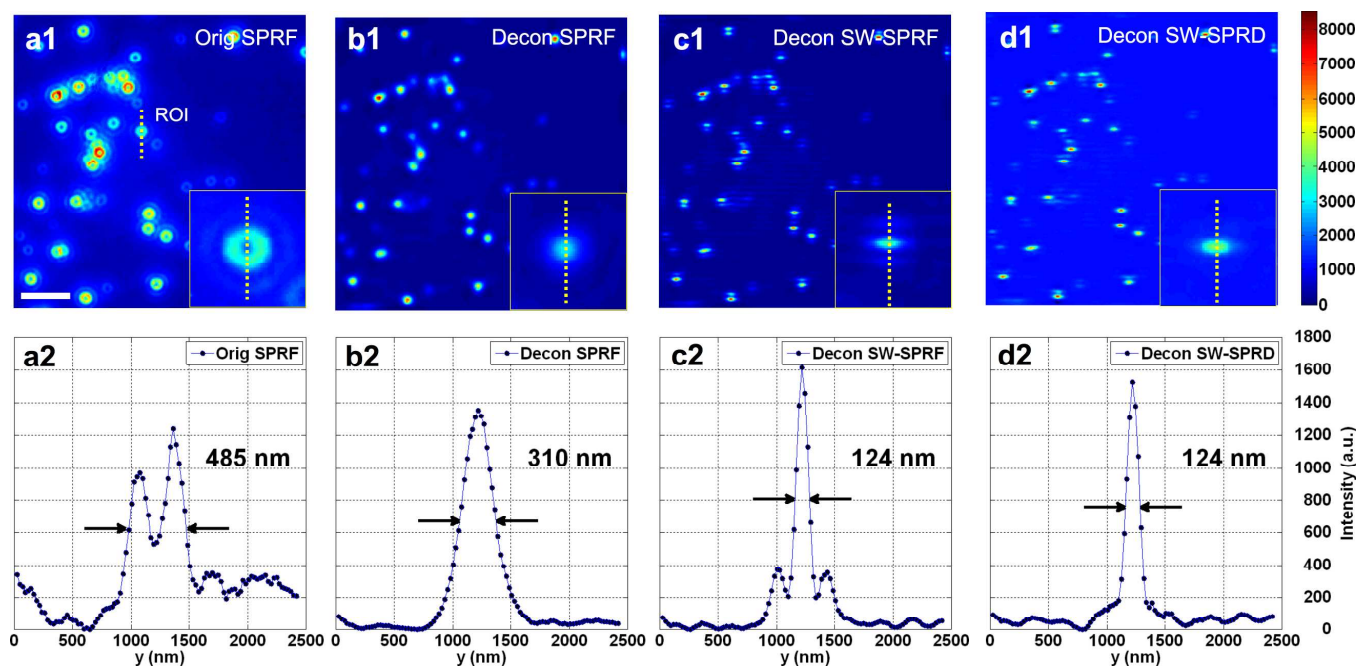


Fig. 3. Extended-resolution imaging with standing-wave surface plasmon resonance fluorescence (SW-SPRF) microscopy in vertical direction (a1) original SPRF image with doughnut-shape PSF, (b1) deconvolved SPRF image, (c1) SW-SPRF image after applying the SW-TIRF algorithm on three deconvolved SPRF images, (d1) SW-SPRF image with linear deconvolution to reduce side lobes; (a2)-(d2) comparison of PSF profiles of various imaging methods at a selected region of interest (ROI). Scale bar: 2 μm . Inset size: 1.3 μm across.

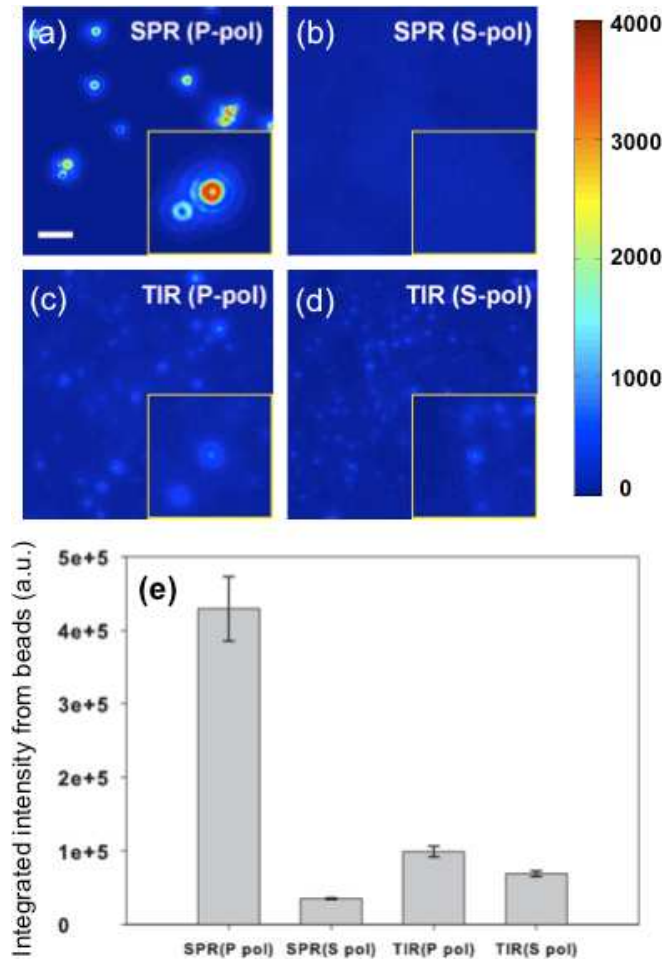


Fig. 4. Comparison of various imaging modes (a)-(d) Images of fluorescent beads under different imaging conditions with the same incident angle, excitation intensity, and exposure time. Scale bar: 2 μm and Inset: 2.5 μm across. (e) Comparison of intensity of fluorescent beads under various imaging modes. (n = 48 each, standard error)